Beitr. Phys. Atmosph., November 1988, p. 330–343
0005–8173/88/04 0330 14 S 3.00/00

The "Papal Front" of 3 May 1987: Modelling of Orographic and Diabatic Effects

D. Heimann

DFVLR-Institut für Physik der Atmosphäre, Oberpfaffenhofen, D-8031 Weßling, FRG.

(Manuscript received May 1988, in revised form accepted September 1988)

Abstract

The remarkable front event over southern Germany on 3 May 1987 is investigated using a simple numerical three-layer model. The model considers the diabatic gain/loss of sensible heat due to condensation of water vapour and evaporation of rain. Additionally, a multiple nesting of smaller fine mesh grid domains into larger coarse mesh domains enables the simultaneous simulation of large scale structures and mesoscale developments.

The simulations show that the Alps cause an evident distortion of the front and especially generate an 'orographic jet'. The behaviour of the cold air in the vicinity of the northern Alpine baseline agrees with the theory of a density current trapped by a mountain range. The numerical simulations yield evidence that diabatic effects of evaporating rain were important for the development of this front. Additionally the eastward propagation of the cold air is intensified by diabatic processes.

Zusammenfassung

Die 'Papstfront' vom 3. Mai 1987: Modellierung orographischer und diabatischer Effekte

Das markante Frontereignis über Süddeutschland vom 3. Mai 1987 wird mit einem einfachen numerischen Dreischichtenmodell untersucht. Das Modell berücksichtigt den diabatischen Gewinn/Verlust an sensibler Wärme aufgrund von Wasserdampfkondensation beziehungsweise Niederschlagsverdunstung. Es ermöglicht zudem die gleichzeitige Behandlung synoptischer Strukturen und mesoskaliger Entwicklungen durch die Nestung hochaufgelöster kleinerer Modellgebiete in größere.

Die Simulationen zeigen, daß die Alpen zu einer auffälligen Verformung der Front und insbesondere zur Ausbildung eines ‚orographischen Jets' führen. Das Verhalten der Kaltluft in der Nähe des Alpennordrandes stimmt mit der Theorie einer Dichteströmung an Bergen überein. Die numerischen Simulationen geben Hinweise darauf, daß die diabtischen Effekte verdunstenden Niederschlags bei der Entstehung dieser Front von Bedeutung sind. Auch wird die Ostwärtsverlagerung der Kaltluft am Nordrand der Alpen durch die Feuchteprozesse verstärkt.

List of symbols

c_{pd}	specific heat capacity of dry air at constant pressure ($c_{pd} = 1004.71\ J\ kg^{-1}\ K^{-1}$)
c_{pv}	specific heat capacity of water vapour at constant pressure ($c_{pv} = 1845.96\ J\ kg^{-1}\ K^{-1}$)
c_w	specific heat capacity of liquid water ($c_w = 4186.80\ J\ kg^{-1} K^{-1}$)
c_F	speed of front progression
c	phase speed of gravity waves
C	condensation rate
Δh	thickness of a layer
Δt	time step
$\Delta x, \Delta y$	horizontal mesh size (cartesian system)
$\Delta\lambda, \Delta\varphi$	horizontal mesh size (geographic system)
E	evaporation rate
ϵ	rotational Froude number
f	Coriolis parameter
Fr	Froude number
g	acceleration of gravity ($g = 9.81\ m\ s^{-2}$)
g'	reduced acceleration of gravity
h	height of a surface
h_0	terrain elevation
H	height scale of the mountains
H_F	height scale of the front
i	grid index in x-direction
j	grid index in y-direction
k	index of layers or levels
L	length scale of the mountains
L_F	length scale of the front

λ	longitude
l_v	specific heat of condensation ($l_v = 2500610\ J\ kg^{-1}$)
N	Brunt Vaisala frequency
N_0	ratio of the height of the front to the height of the mountain
N_1	ratio of inertia to earth rotation
N_2	ratio of kinetic to potential energy
N_3	ratio of mountain slope to frontal slope
ν	index of time step
p	pressure
π	Exner function
φ	latitude
q_v	specific humidity
Q_v	specific saturation humidity
q_r	specific content of rain drops
R	Rossby radius
R_E	radius of earth ($R_E = 6371.231$ km)
r_v	mixing ratio
R_d	gas constant of dry air ($R_d = 287.06\ J\ kg^{-1}\ K^{-1}$)
R_v	gas constant of water vapour ($R_v = 461.51\ J\ kg^{-1}\ K^{-1}$)
ρ_d	density of air
Ro	Rossby number
t	time
T	temperature
Θ	potential temperature
Θ_v	virtual potential temperature
U	scale of horizontal velocity
u, v	horizontal wind components
u_g, v_g	horizontal components of the geostrophic wind
w	vertical velocity (cartesian system)

Abbreviations

FRG	Federal Republic of Germany
MSL	above mean sea level
UTC	universal time coordinated

1 Introduction

On 3 May 1987 a very intense cold front crossed southern Bavaria connected with strong winds, heavy rain and snow, and even embedded thunderstorms. This front was named 'papal front' since pope John Paul II, who was visiting München at this day, was hindered to use a helicopter for his transfer to Augsburg due to severe turbulence associated with this front. Heimann and Volkert (1988) evaluated routine data to analyze this case in detail.

During this analysis two major questions came up:

1. Did the Alps cause the accelerated eastward propagation of this front?
2. Was diabatic cooling due to evaporating rain and melting snow responsible for the development of the front?

The influence of the Alps on the movement of cold fronts has been described by Steinacker (1987). By analyzing isochrones he found various froms of frontal behaviour which reached from a slight retardation to a total blocking. Studies of Parish (1982) and Colquhoun et al. (1985) show that the blocking effect leads to an acceleration along the mountains. Parish used radar and aircraft measurements and found the 'barrier jet' along the Californian Sierra Nevada as a consequence of blocked advection of cold air. Colquhoun et al. described the Australian 'Southerly Burster', an active cold front which is blocked by the coastal mountains of New South Wales, but accelerated along the coast. Baines (1980) explained the 'Southerly Burster' as a gravity current trapped by the coastal mountain range. Egger and Haderlein (1987) used the term 'orographic jet' for this phenomenon and discussed the relationship between the speed of the jet's nose and parameters of the approaching cold air.

The frontogenetic effect of diabatic processes has been discussed by Kurz (1982). He analyzed a case where a new front formed at the leading edge of a large belt of precipitation ahead of a synoptic-scale cold front. Cooling due to evaporating rain at the rear side, and heating due to solar radiation within the almost cloud-free warm sector strengthened the horizontal temperature gradient in this case.

On 3 May1987 the synoptic-scale cold front was not connected with significant precipitation, but a new area of rain formed ahead of the upper level trough which followed the front some hundred kilometers west of it. The 'papal front' developed at the leading edge of this area of precipitation. It rapidly propagated eastward and eventually caught up with the preceding synoptic-scale cold front.

Although the analysis already gave some hints for affirmative answers to the questions posed above, one can expect additional evidence from model simulations. They allow to separate the influence of diabatic processes and orography.

The paper describes the model in Chapter 2. Section 3.1 explains the strategy of the simulations and Section 3.2 deals with the model initialization and the synoptic development. The orographic influence on the frontal system, especially the development of an 'orographic jet', is discussed in Section 3.3, and compared with theoretical estimates in Section 3.4. Finally, the importance of diabatic heat exchange is addressed in Section 3.5.

2 The Model

2.1 Model Conception

A simple but effective approach for the numerical exploration of frontal dynamics is the application of the shallow-water equations to vertically isentropic layers with free and unpermeable surfaces. Each layer represents a specific air mass. Such surfaces of layers intersecting with the ground can be interpreted as fronts. A one-layer model of this kind has been used by Kasahara et al. (1965) to investigate the movement of fronts under the influence of a synoptic-scale baroclinic wave. While Kasahara et al. neglected the dynamics of the overlying warm air, it is considered by Grammeltvedt (1970) who added a second active model layer. More recently Egger (1987) and Egger and Haderlein (1987) incorporated orography to investigate mesoscale mountain effects such as the distortion of a cold front and the development of an 'orographic jet'.

Also this study uses the rather simple conception of the shallow-water model, because it is economic and has a limited number of free model parameters. For a better adaptation to the actual questions the model figuration was extended by

- using three model layers instead of one or two;
- providing the possibility of multiple nesting;
- considering the diabatic effects of condensation and evaporation.

The geometric structure of the present model (shortly addressed as FRONTOM which stands for 'front and orography'-model) can be related to the real structure of tropospheric air masses and fronts as follows:

The lowest layer conforms to a 'cold air' mass. The surface of this layer forms a material frontal face. Its intersecting line with the ground represents the 'surface front'. The model front can be interpreted as a 'cold front', if the lowest model layer advances, or as a 'warm front', if it retreats. The second layer conforms to a 'warm air' mass which either touches the ground or overlies the cold air. The upper tropospheric air is represented by the third model layer. Its surface forms the model lid and is defined as the 300 hPa level. Above this surface the model atmosphere is assumed to be in geostrophic balance. Hence, the pressure at the model lid does not change with time. The vertical model structure is schematically illustrated in Figure 1.

The model is based on the equations of a hydrostatic, non-divergent, and frictions-less atmosphere. The first two assumptions are quite indisputable in the considered scale. Friction, of course, is known as an important factor of frontal dynamics (e.g. Ball, 1960 and Garrat, 1986). Recently Egger (1988) discussed stationary two-dimensional solutions of the flow in a two-layer

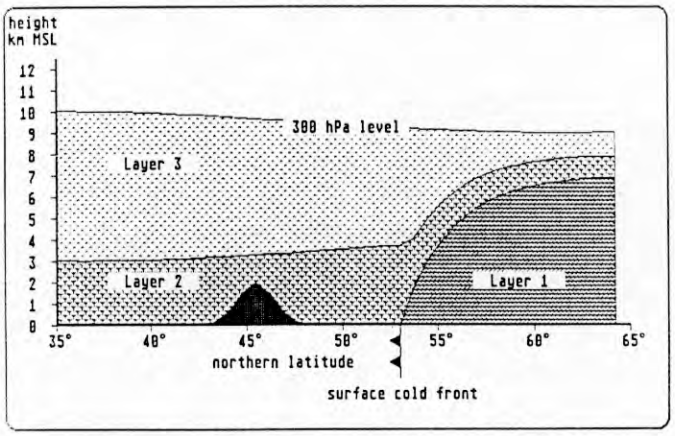

Figure 1 Schematic illustration of the vertical model structure

fluid system. He found that the frontal face becomes steeper with increasing friction. This is in agreement with experimental runs of FRONTOM during which a bulk formula for stress was invoked in the lowest model layer. However, in this study it was given preference to a friction-less formulation particulary because a no-slip condition would depend on a drag coefficient which has to be prescribed more or less arbitrarily.

The fixed horizontal grid and the division into layers define homogeneous model boxes. The potential temperature Θ and the specific humidity q_v are time dependent variables within each box. Surplus water vapour is immediately condensated and converted into rain. The release of latent heat increases the potential temperature of the corresponding model box. Precipitation can partly evaporate in the underlying boxes where the potential temperature decreases due to the consumption of sensible heat.

2.2 Model Equations

The equations are formulated for the layers $k = 1,\ldots,3$ (for u, v, Θ, q_v), or for the surfaces $k = 0,\ldots,3$ (for w, π). All model variables depend on the horizontal coordinates x and y.

Equations of motion

$$\frac{\partial u_k}{\partial t} = -u_k \frac{\partial u_k}{\partial x} - v_k \frac{\partial u_k}{\partial v} + f v_k - c_{pd}\,\Theta_{vk} \frac{\partial \pi_k}{\partial x} - g \frac{\partial h_k}{\partial x} + g \frac{h_k - h_{k-1}}{2\Theta_{vk}} \frac{\partial \Theta_{vk}}{\partial x} \quad (1)$$

$$\frac{\partial v_k}{\partial t} = -u_k \frac{\partial v_k}{\partial x} - v_k \frac{\partial v_k}{\partial y} - f u_k - c_{pd}\,\Theta_{vk} \frac{\partial \pi_k}{\partial y} - g \frac{\partial h_k}{\partial y} + g \frac{h_k - h_{k-1}}{2\Theta_{vk}} \frac{\partial \Theta_{vk}}{\partial y} \quad (2)$$

for layers $k = 1,\ldots,3$. $h_{k=0}$ is the terrain elevation.

Hydrostatic equation

$$\pi_{k-1} = \pi_k + \frac{g}{c_{pd}\,\Theta_{vk}}\,(h_k - h_{k-1}) \qquad (3)$$

for surfaces k = 1, ..., 3.

π_3 has a constant value of 0.71 which conforms to a pressure p_3 = 300 hPa at the model lid. $\pi_{k=0}$ is the Exner function at ground level ($h_{k=0}$).

Equation of continuity

a) Determination of the vertical velocity:

$$w_k = w_{k-1} - \left(\frac{\partial u_k}{\partial x} + \frac{\partial v_k}{\partial y}\right)\cdot(h_k - h_{k-1}) + (u_k - u_{k-1})\,\frac{\partial h_{k-1}}{\partial x} + (v_k - v_{k-1})\,\frac{\partial h_{k-1}}{\partial y} \qquad (4)$$

for surfaces k = 1, ..., 3 with $u_{k=0} = v_{k=0} = w_{k=0} = 0$ as the boundary condition at the ground ($h_{k=0}$).

b) Determination of the tendency of the surface heights:

$$\frac{\partial h_k}{\partial t} = w_k - u_k\,\frac{\partial h_k}{\partial x} - v_k\,\frac{\partial h_k}{\partial y} \qquad (5)$$

for surfaces k = 1, ..., 3.

Temperature equation

$$\frac{\partial \Theta_k}{\partial t} = -u_k\,\frac{\partial \Theta_k}{\partial x} - v_k\,\frac{\partial \Theta_k}{\partial y} + \frac{l_v\,(C_k - E_k)}{c_{p,k}\,\dfrac{\pi_k + \pi_{k-1}}{2}} \qquad (6)$$

with

$$c_{p,k} = \frac{(1 - q_{v,k})\,c_{pd} + q_{v,k}\,c_{pv} + q_{r,k}\,c_w}{1 + q_{r,k}}$$

for layers k = 1, ..., 3.

Humidity equation

$$\frac{\partial q_{v,k}}{\partial t} = -u_k\,\frac{\partial q_{v,k}}{\partial x} - v_k\,\frac{\partial q_{v,k}}{\partial y} - C_k + E_k \qquad (7)$$

for layers k = 1, ..., 3.

General definitions

Coriolis parameter:

$$f(\varphi) = f_0 \cdot \sin(\varphi) \text{ where } f_0 = 1.4584 \cdot 10^{-4}\,s^{-1}$$

Exner function:

$$\pi = (p/p_0)^{R_d/c_{pd}} \text{ where } p_0 = 10^5 \text{ Pa}$$

virtual potential temperature:

$$\Theta_v = \Theta\left(1 + \frac{R_d}{R_v}\,q_v\right)$$

2.3 Incorporation of Diabatic Processes

The representation of condensation and evaporation can only be crude in a model that resolves the troposphere by only three layers. However, the following procedure is used to determine the rates of conversion from the gas phase to the liquid phase and vice-versa. Under the assumptions

$$r_v \approx q_v$$

$$l_v \neq l_v(T)$$

$$\frac{1}{\pi_{k-1} - \pi_k}\int_{\pi_{k-1}}^{\pi_k} r_{v,k}(\pi)\,d\pi \approx \approx \exp\left[\frac{1}{\pi_{k-1} - \pi_k}\int_{\pi_{k-1}}^{\pi_k} \ln r_{v,k}(\pi)\,d\pi\right]$$

a bulk expression for the maximum (saturation) content of water vapour $Q_{v,k}$ in a model box of layer k was derived by vertically integrating the Clausius-Clapeyron equation. It reads

$$r = \exp\left[c_1 + \frac{c_2\,(\pi_k \ln \pi_k - \pi_{k-1} \ln \pi_{k-1}) + c_3\,\dfrac{\ln(\pi_k/\pi_{k-1})}{\Theta_k}}{\pi_{k-1} - \pi_k}\right]$$

$$Q_{v,k} = \frac{r}{1 + r} \qquad (8)$$

where

$$c_1 = \ln\frac{R_d}{R_v} + c_{pd}/R_d + 14.7369$$

$$c_2 = c_{pd}/R_d$$

$$c_3 = l_v/R_v$$

$Q_{v,k}$ depends on the potential temperature Θ_k within the respective box and on the pressure at its bottom and top faces (π_{k-1}, π_k).

In the case of over-saturation ($q_{v,k} > Q_{v,k}$) the excess water vapour is condensated immediately and converted to rain:

$$C_k = \max\left[\frac{q_{v,k} - Q_{v,k}}{\Delta t}, 0\right]$$

$$q_{r,k} = \max\left[q_{v,k} - Q_{v,k}, 0\right]$$

for all layers k = 1, ..., 3.

Thus, the model does not account for clouds. The generated rain falls into the lower layers where it may

partly evaporate in case of under-saturation:

$$E_\kappa = C_0 \frac{\min [q_r, \max [Q_{v,\kappa} - q_{v,\kappa}, 0]]}{\Delta t}$$

$$q_{r,\kappa} = q_{r,\kappa+1} - E_\kappa \Delta t$$

This procedure is carried out for all layers $\kappa = k - 1, \ldots, 1$ at the same time step. C_0 is a factor of evaporation which must be prescribed. During all model runs C_0 was arbitrarily set to 0.5. Only precipitation that has not been evaporated will reach the ground.

The introduced scheme allows a rough estimation of the diabatic heat exchange associated with condensation and evaporation. Realistic values for the amount of precipitation cannot be expected, of course. This is a consequence of the model conception of vertically uniform layers. In reality a uniformly cooled or lifted air parcel with $\partial\Theta/\partial z = 0$ and $\partial q_v/\partial z = 0$ would reach over-saturation which starts locally at its top. In the model condensation cannot take place before the bulk saturation humidity becomes smaller than the actual humidity, i.e. $Q_{v,k} < q_{v,k}$.

2.4 Numerical Procedure

FRONTOM uses a staggered grid. The scalars h_k, π_k, Θ_k, $q_{v,k}$ are defined at the mesh centres, whereas the wind components u_k and v_k are placed at the middle of the mesh boundaries. The potential temperature Θ_k and the specific humidity $q_{v,k}$ refer to the entire vertical extent of a model layer, while the heights h and the Exner function π are related to the surfaces of the layers.

A semi-implicit two-step procedure, the so called 'Euler backward' scheme, is employed for the temporal integration of the prognostic equations. With $\varphi = (u, v, h, \Theta, q_v)$ the two steps read:

$$\varphi^{\nu*} = \varphi^\nu + \Delta t \cdot F_\varphi (\varphi^\nu, \ldots)$$

$$\varphi^{\nu+1} = \varphi^\nu + \Delta t \cdot F_\varphi (\varphi^{\nu*}, \ldots)$$

where the indices ν and $\nu + 1$ denote consecutive time steps. $\nu*$ is a provisional stage of the prognostic model variables. F_φ stands for the actual tendency of φ. It is derived from the model variables at stage ν or $\nu*$, respectively.

All spatial derivatives with the exception of advective terms are approximated by central differences. Upstream differences are used in the advective terms. Due to its damping property this scheme keeps the solution stable and substitutes explicit horizontal diffusion.

2.5 Nesting and Boundary Conditions

The model provides the possibility of a multiple nesting of smaller grid domains into larger ones. In this way it is possible to cover a wide range of scales with one model.

During each simulation period the synoptic-scale modelling is carried out in a domain A, which has to be chosen large enough to resolve the relevant synoptic steering features such as baroclinic waves. Within prescribed or automatically determined sub-periods the same model is run simultaneously in a nested domain B with higher resolution. Analogous to this procedure an even better resolved domain C can be activated within domain B. The vertical structure of the model is not affected by the nesting.

The coupling of the nested domains is carried out by prescribing the tendencies of the prognostic variables u_k, v_k, h_k, Θ_k, $q_{v,k}$ at the boundary meshs of the subordinated domain. The tendencies are derived from the appropriate meshs of the superposed domain. The method of interpolation from the larger to the smaller meshs is examplarily described in Figure 2 for the scalar variables. The analogous procedure is used for the wind components. In the literature the described kind of nesting is called 'one-way'-nesting, 'passive' nesting, or 'parasitary' nesting, e.g. Clark and Farley (1984), Zhang et al. (1986). The method does not provide a feedback from the smaller domain to the larger one.

Tendencies of the boundary values of the outermost domain A are determined internally using radiation conditions. The procedure is examplarily sketched for the western boundary, i.e. $i = 1$, and the time level $\nu + 1$:

$$\frac{\varphi_{i=1}^{\nu+1} - \varphi_{i=1}^{\nu}}{\Delta t} = -c_\varphi \frac{\varphi_{i=2}^{\nu} - \varphi_{i=1}^{\nu}}{\Delta x}$$

with

$$c_\varphi = \min \left[-\frac{\varphi_{i=2}^{\nu+1} - \varphi_{i=2}^{\nu}}{\varphi_{i=3}^{\nu} - \varphi_{i=1}^{\nu}} \cdot \frac{2\Delta x}{\Delta t}, 0 \right]$$

and $\varphi_k = (u_k, v_k, h_k, \Theta_k, q_{v,k})$.

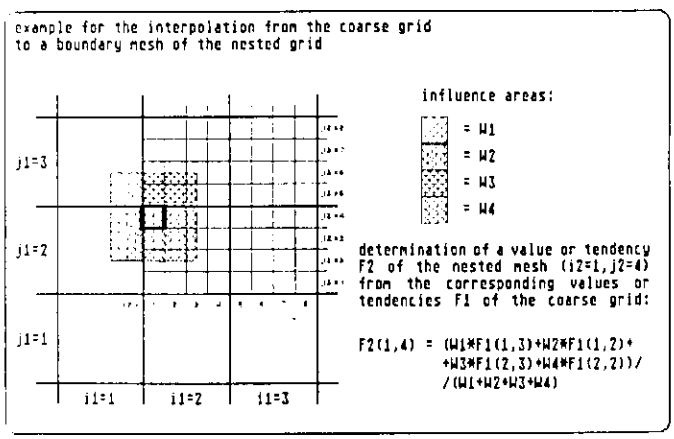

Figure 2 Scheme of nesting and interpolation from a coarse grid to a fine grid

2.6 Definition of the Nested Model Domains

For the real case simulations the meshes of the FRONTOM domains are defined on a geographic net. Within each domain the mesh widths $\Delta\lambda$ and $\Delta\varphi$ are constant.

The usage of geographic coordinates requires additional metric terms in eqs. (1), (2) and (4). They read

$$\frac{\partial u_k}{\partial t} = \ldots + u_k v_k \frac{\tan\varphi}{R_E} \quad \text{in (1)}$$

$$\frac{\partial v_k}{\partial t} = \ldots - u_k u_k \frac{\tan\varphi}{R_E} \quad \text{in (2)}$$

$$w_k = \ldots + v_k \frac{\tan\varphi}{R_E}(h_k - h_{k-1}) \quad \text{in (4)}$$

The mesh sizes in the metric system are calculated as:

$$\Delta x(\varphi) = R_E \cos\varphi \, \Delta\lambda$$

$$\Delta y = R_E \Delta\varphi$$

According to the common scale definitions of atmospheric phenomena (Orlanski, 1975) the model domains are defined to resolve atmospheric structures as follows:

Domain A: macroscale β or synoptic scale
(baroclinic waves, high and low pressure systems, synoptic-scale fronts)

Domain B: mesoscale α
(flow over or around mountains, foehn, orographic distortion of fronts)

Domain C: mesoscale β
(density currents, channelling, 'orographic jets')

For this study the size of the outermost model domain A was chosen to be of 60° west-east extension and of 30° south-north extension. This allows the resolution of the planetary zonal wave number 6, which seems to be sufficient for simulations not exceeding a period of 24 hours. The grid domain includes 40 × 40 meshes. The consequent grid spacing is 1.5° in west-east direction, and 0.75° in south-north direction, or between 70 and 135 km in the metric sense. The subordinated model domains B and C also consist of 40 × 40 grid meshs, but their grids are condensed by the factor 4 relative to the respective next outer domain. The use of three nested domains enables a resolution of 20 to 30 km in domain B, and of 5 to 7 km in domain C.

The orographic data are taken from a digital geographic data base as mean values of the grid meshs. All domain specifications are summerized in Table 1. The corresponding maps are presented in Figure 3.

3 Numerical Simulations of the 'Papal Front' Case

3.1 Aim and Strategy of Simulations

The main objective of the numerical simulations of the 'papal front' case is the influence of both, the diabatic processes and the orography, on the development, the intensification, and the deformation of the fronts north of the Alps on 3 May 1987.

The analyzed situation (see Heimann and Volkert, 1988) is summarized in Figure 4. At 12 UTC the synoptic-scale cold front of the southern Scandinavian low, subsequently called 'Front 1', has reached the western parts of the Alps. Its position over the northern Alpine foreland is almost stationary. The surface potential temperature drops by about 6 K across this front. After 06 UTC a second zone of large horizontal temperature gradient has formed west of the Rhine river. By 12 UTC this zone had proceeded to the line Lake of Constance – Stuttgart. It belongs to a second cold front which has a more regional character and can be analyzed

Table 1 Specifications of the model domains A, B, and C.

	domain A	domain B	domain C
western boundary	20° W	2.5° E	10° E
eastern boundary	40° E	17.5° E	13.75° E
southern boundary	35° N	42.5° N	47° N
northern boundary	65° N	50° N	48.875° N
number of meshs	40 × 40	40 × 40	40 × 40
$\Delta\lambda$	1.5°	0.375°	0.09375°
$\Delta\varphi$	0.75°	0.1875°	0.046875°
Δx	70, ..., 135.7 km	26.8, ..., 30.8 km	6.9, ..., 7.1 km
Δy	82.8 km	20.8 km	5.2 km
minimum terrain elevation	0	0	314 m MSL
maximum terrain elevation	2226 m MSL	2895 m MSL	2829 m MSL
maximum slope of terrain	13 m/km	64 m/km	149 m/km
	1:77	1:16	1:7

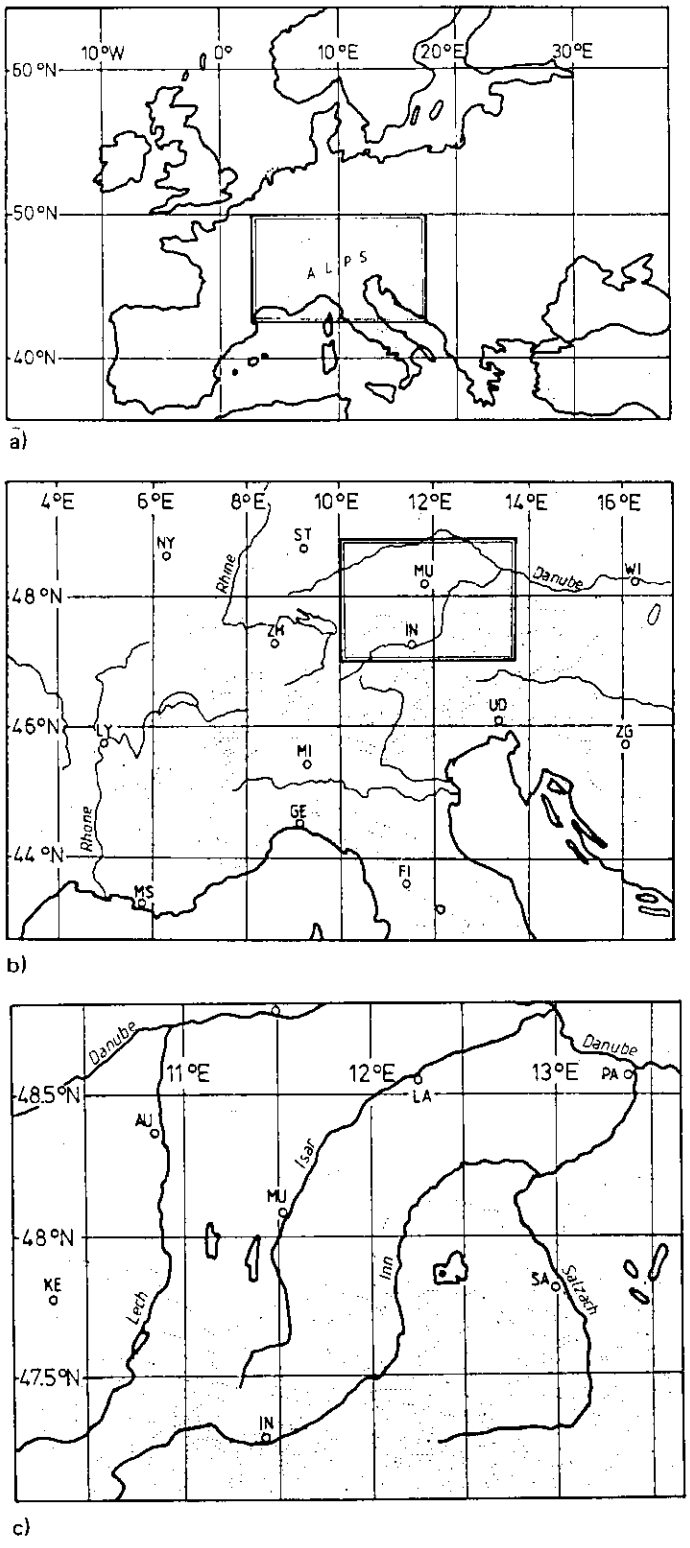

Figure 3 Maps of nested model domains (without the respective boundary meshs).
(a) Top: Domain A. The contour interval of the terrain elevation is 500 m. The inner frame encloses model domain B.
(b) Middle: Domain B. The contour interval of the terrain elevation is 500 m. The inner frame encloses model domain C.
(c) Bottom: Domain C. The contour interval of the terrain elevation is 250 m. AU: Augsburg/FRG, FI: Firenze/Italy, GE: Genova/Italy, IN: Innsbruck/Austria, KE: Kempten/FRG, LA: Landshut/FRG, LY: Lyon/France, MI: Milano/Italy, MS: Marseille/France, MU: München/FRG, NY: Nancy/France, PA: Passau/FRG, SA: Salzburg/Austria, UD: Udine/Italy, WI: Wien/Austria, ZG: Zagreb/Yugoslavia, ZH: Zürich/Switzerland

only between Switzerland and the Main river. This front was referred to as 'papal front', but will be called 'Front 2' in the following for convenience. It quickly intensified and rapidly crossed southern Germany and northern Austria where it caught up with Front 1. A noteworthy feature is the pool of cold air behind Front 2. It coincides with an area of precipitation which directly followed this front. Potential temperatures below 6 °C cannot be explained from advection in this case. Instead, diabatic cooling by evaporating rain and melting snow is surmised to be the reason.

The movement of Front 2 is illustrated by hourly isochrones in Figure 4b. The significant acceleration of the front along the Alpine baseline and the formation

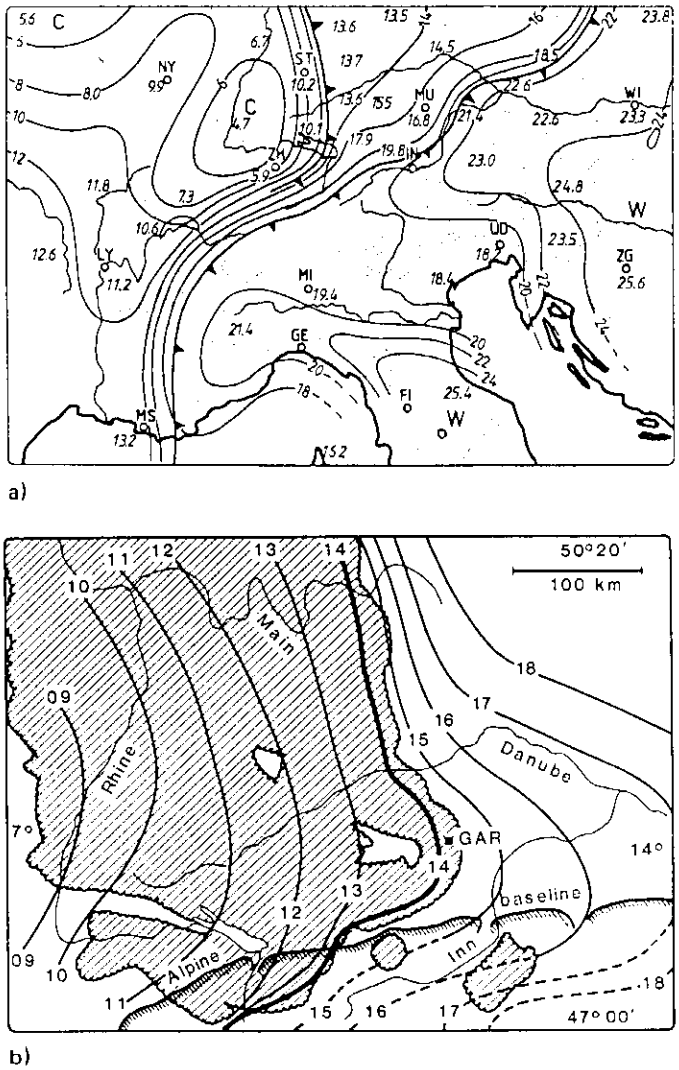

Figure 4
(a) Top: Analysis of surface potential temperature (°C) and positions of cold fronts on 3 May 1987 at 12 UTC.
(b) Bottom: Hourly isochrones of the analyzed positions of Front 2 between 09 and 18 UTC. At 15 UTC Front 2 has merged into the preceding Front 1. The hatched area indicates the region with cloud top temperatures of below 40 °C at 14 UTC adapted from an infrared satellite image. (Source: Heimann and Volkert, 1988)

of a nose-like shape of the surface front line are suspected to be caused by the Alpine topography. Similar developments have been observed along other mountain ranges like the Australian Alps (Colquhoun et al., 1985) or the Pyrenees (Hoinka and Heimann, 1988). Since the observed wind velocities had a maximum near the northern rim of the Alps, the behaviour of the front may be addressed as an 'orographic jet'.

The numerical experiments are designed as to allow separating the influences of diabatic heat exchange and orography, respectively. The use of three nested grid domains ensures the explicit treatment of the synoptic structures which are responsible for large scale lifting and precipitation, and the resolution of mesoscale processes as well.

Three model runs have been performed:

I. Run I with diabatic processes and real orography
   Domain A: 00 UTC – 24 UTC
   Domain B: 06 UTC – 18 UTC
   Domain C: 06 UTC – 13 UTC

II. Run II with diabatic processes, but with 'flat' orography
   Domain A: 00 UTC – 18 UTC
   Domain B: 06 UTC – 18 UTC
   'Flat' orography in this run means that the maximum terrain elevation is limited to 500 m MSL. The ‚Alps' then reduce to a plateau which joins the northern Alpine foreland without a step.

III. Run III without diabatic processes, but with real orography
   Domain A: 00 UTC – 18 UTC
   Domain B: 06 UTC – 18 UTC

The orographic influence can be assessed by interpreting the differences between the runs I and II. On the other hand, the evaluation of the differences between the model runs I and III enables one to estimate the importance of diabatic effects.

3.2 Initialization and Synoptic Development

All three model runs were initialized with the European radiosonde data of 3 May 1987, 00 UTC. From these data the heights of two isentropic levels, the 286 K level and the 307 K level were determined at each station. The 286 K level was chosen to represent the frontal surface of the synoptic-scale Front 1, which is related to the surface of the lowest model layer (h_1). The selection of the 307 K level as an equivalent of the initial surface height of the second model layer (h_2) was a result of systematic tests during which the potential temperature was varied from 301 to 309 K in steps of 2 K. The initialization with the 307 K level led to the most realistic distribution of the large-scale precipitation. Furthermore, the height of the 300 hPa level was derived from the aerological data. It is used for the initial surface height of the third model layer (h_3).

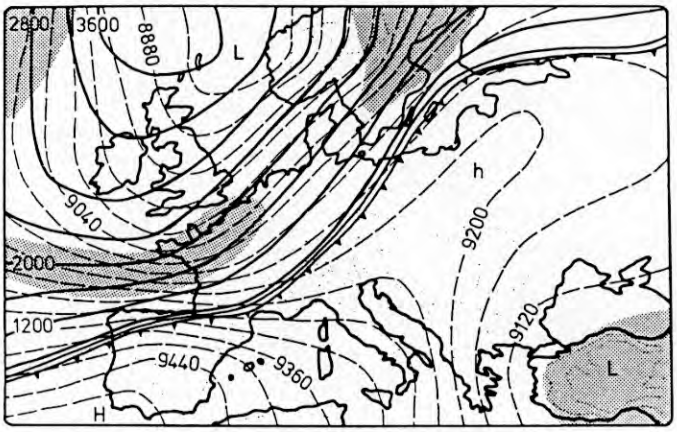

Figure 5 Model domain A, 3 May 1987, 00 UTC:
Initial state of the model runs I, II, and III.
The solid lines indicate the thickness of the lowest model layer (in m). The surface front is plotted with front symbols. The broken lines represent the surface height of the upper most model layer (in m MSL), which coincides with the 300 hPa level. The shaded area indicates regions with a relative humidity of 80 % or more within model layer 2.

The fields of the surface heights (h_k), the pressure values at the surfaces (π_k), and the vertically integrated specific humidities within the layers ($q_{v,k}$) were horizontally interpolated from the locations of the aerological stations to the mesh centres using distance dependent weights.

The virtual potential temperatures were derived for each mesh and in each layer, i.e. for all model boxes, by

$$\Theta_{v,k} = \frac{g}{c_{pd}} \frac{h_k - h_{k-1}}{\pi_{k-1} - \pi_k} \tag{9}$$

The initial wind field is calculated assuming geostrophic balance in each model layer while neglecting orographic effects. The orography is smoothly added during the first three hours of integration by 'diastrophy', i.e. by blowing up the orography linearly with time.

Figure 5 depicts the initial state at 00 UTC. The surface of the lowest model layer intersects with the ground on a line reaching from northern Spain via southern France, south-western Germany towards the Baltic Sea and Finland. This line agrees well with the position of the synoptic-scale cold front in the published weather charts of this time. The thickness of the lowest model layer increases to 3700 m above the Norwegian Sea.

By 12 UTC the cold air mass of model layer 1 has passed through the gap in between the Pyrenees and the Alps towards the Mediterranean Sea (Figure 6a). Along the northern rim of the Alps the cold air has propagated also, while further to the north it remained almost

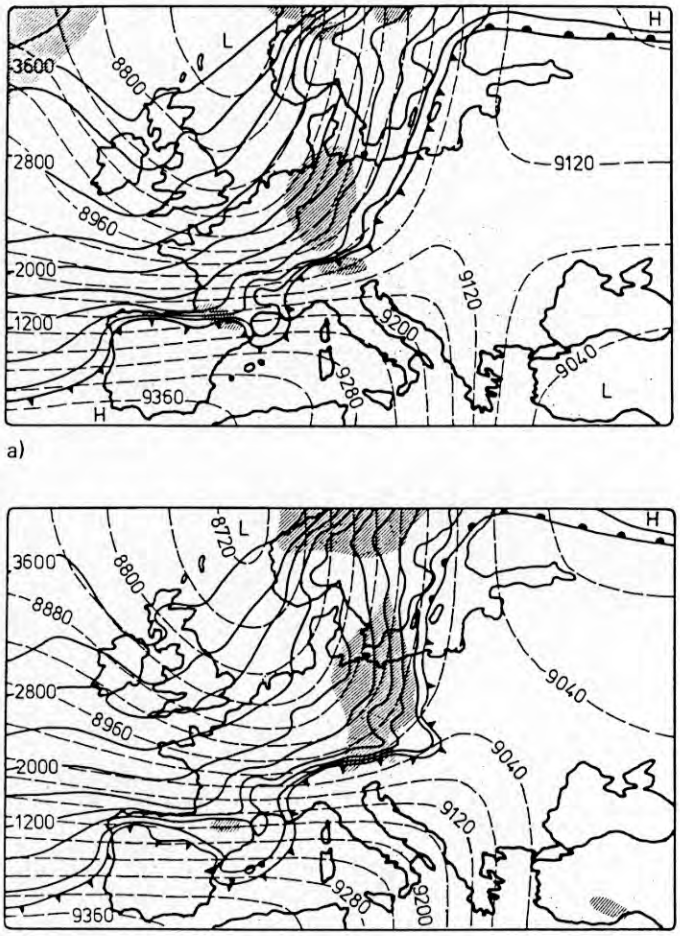

Figure 6 Simulated synoptic-scale development in model domain A, run I:
The solid lines depict the thickness of the lowest model layer (in m). The surface front is plotted with front symbols. The broken lines represent the surface height of the uppermost model layer (in m MSL). The hatched area shows the region with simulated precipitation of 0.05 mm or more during the last hour.
(a) Top: 3 May 1987, 12 UTC (after 12 hours of simulation)
(b) Bottom: 3 May 1987, 18 UTC (after 18 hours of simulation)

stationary. The 300 hPa trough, i.e. the surface of model layer 3, has shifted to the east. The model suggests that the precipitation area ahead of it was formed as a consequence of positive vorticity advection. This is supported by detailed output analyses of ECMWF's general circulation model. They show an area of strong positive vorticity advection moving with its centre from northern France (00 UTC) to south-west Germany (12 UTC). The dynamic effect of positive vorticity advection was not compensated by cold air advection north of the Alps, since the main movement of the cold air behind Front 1 was directed towards the Mediterranean. As a consequence large-scale rising was dominant in this area, which coincides quite well with a rapidly developing comma-like cloud formation in the METEOSAT infrared images. Further details of the synoptic-scale dynamics of 3 May 1987 are given by Heimann and Volkert (1988).

In the FRONTOM run the precipitation is not attached to front 1 but lags it by about 200 km. This is in agreement with observations. It is remarkable that run II (with flat orography) did not produce rain in the Alpine foreland east of the Black Forest, while run I (with real orography) even brought about a precipitation maximum around Lake of Constance.

After 12 UTC the leading edge of model layer 1, i.e. front 1, has reached Hungary and penetrated further to the Mediterranean, while it was still retained by the Alps and the Pyrenees (Figure 6b). North of the 55th parallel the front became even retrograde taking the characteristics of a northwestward moving warm front. The nose-like shape of the front north of the Alps is evident.

The mesoscale development of front 1 and the generation of front 2 will be discussed in the following sections by focussing on model domains B and C.

3.3 Development of the 'Orographic Jet'

The role of the Alps is evident in Figure 7. The difference vectors (run I – run II) exhibit the typical anticyclonic acceleration due to orography, which is explained by the conservation law of potential vorticity. This behaviour was also found in model calculations by Haderlein (1986) or Schumann (1987). In the case with real orography the flow is blocked in the western part of the domain, so that the front lags behind by up to 400 km. North of the Alps the cold air propagates faster with fully represented mountains. Since the front hangs back further to the north at approximately the same position as in run II, it took the shape of a nose close to the Alps. Note that a similar looking nose-like curvature of the front in the south-westernmost part of model domain B is an influence of the Pyrenees, imported from model domain A, rather than an effect of the Alps.

The nose-like deformation of the front north of the Alps can be explained in terms of the model physic as follows: The west-east orientated mountain barrier blocks the southward motion of the cold air leading to a vanishing v_1 in Equation 1. The air flow is no longer in geostrophic balance as the acceleration of u_1 is now mainly determined by inertia and pressure forces. Near the front the pressure force is dominated by the discontinuous density at the inclined surface separating model layers 1 and 2. Thus, the cold air of the model layer 1 accelerates along the barrier towards the east like a trapped gravity flow. Since the acceleration only acts within a strip of certain width along the barrier it brings about the nose-like shape of the front.

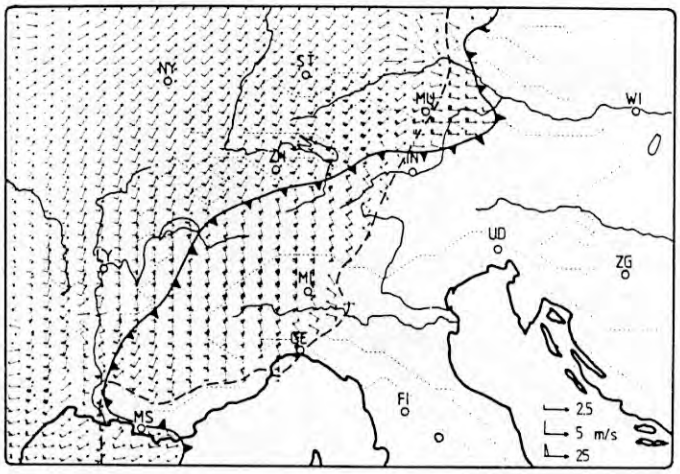

a)

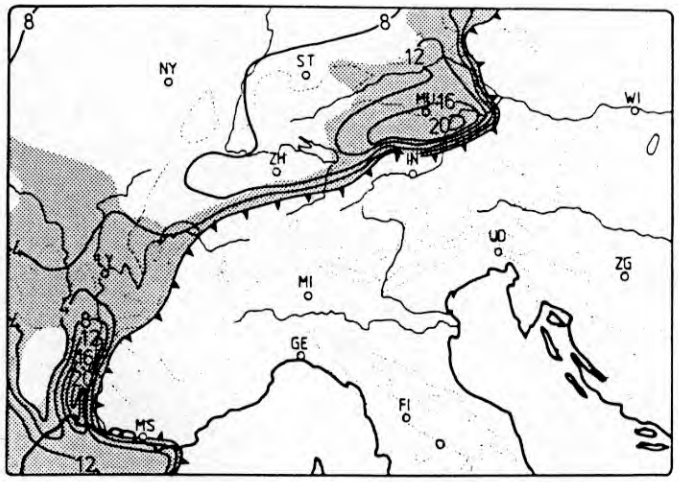

b)

Figure 7 Model domain B, 3 May 1987, 12 UTC:
(a) Top: Difference vectors of the simulated winds of the model layer 1 between run I with real orography and run II with 'flat' orography ($\vec{v}_{1,I} - \vec{v}_{1,II}$). The line with front symbols indicates the position of Front 1 simulated in run I, the broken line shows the position of this front simulated in run II.
(b) Bottom: Simulated velocity in the model layer 1 for run I ($|\vec{v}_{1,I}|$ in m/s). The shaded area shows the region where the percentage of the ageostrophic velocity part is 50 % or more.

The wind velocity in model layer 1 is evidently increased north of the Alps with a maximum immediately behind the front in the area of the frontal nose (Figure 7b). In the following this will be addressed as 'orographic jet'. A second wind maximum is found in the Rhone valley representing the well known 'mistral'. Figure 7b also gives the percentage of the ageostrophic part of the wind speed. In accordance to the theory of trapped gravity currents the flow is out of geostrophic equilibrium in the region of the frontal nose.

The temporal development of the 'orographic' jet is displayed in Figure 8. The vertical cross section along 11° E shows the cold air mass of model layer 1 approaching from the northwest. By 12 UTC it has

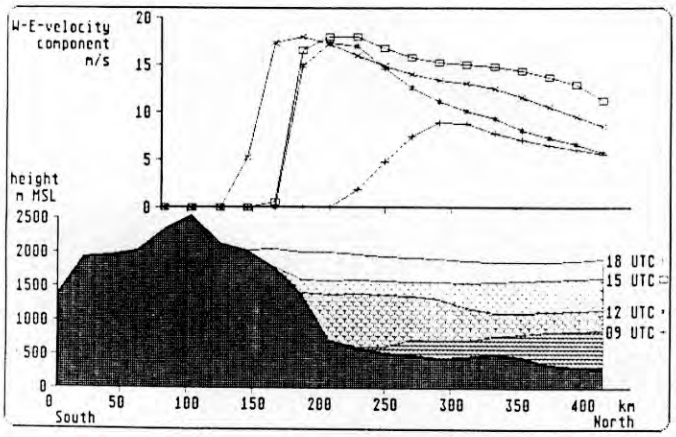

Figure 8 Model domain B, 3 May 1987, run I:
South-north cross section along 11° E of the surface height and the west-east velocity component u_1 of model layer 1 at 09, 12, 15, and 18 UTC.

reached the Alpine baseline. At this time the section cuts through the head of the front and the orographic jet is most pronounced. The surface of the cold air is vaulted by around 300 m within a distance of about 100 km north of the Alps. The mountain parallel component of the wind reaches 15 m/s close to the Alps, but decreases to less than 10 m/s further away. During the consecutive hours the frontal head moves out of the cross section and the surface of the cold air levels in south-north direction. The west-east wind component has still its maximum close to the Alps, but the jet-like contrast of speed has decreased.

For a more detailed inspection of the frontal nose we turn to the results of model domain C. At 12 UTC the region of the orographic jet is roughly enclosed by the 16 m/s isotach (Figure 9a). Although we find the maximum speed of 25 m/s immediately behind the front, secondary maxima follow in the wake of the front along the Alpine baseline. It is evident that the velocity is smaller near exits of major Alpine valleys like the Inn valley. The cold air partly penetrates into these valleys and the consequent divergence decreases the speed. For the same reason wind speed maxima are found near the steepest slops of the mountain rim.

Half-hourly isochrones of the front show clearly the formation of the progressing frontal nose between 10 and 12 UTC (Figure 9b). An estimation of the propagation speed of the front yields values of 17 m/s near Kempten, 21 m/s near Salzburg, but not more than 10 m/s along the northern boundary of domain C. At 12 UTC the propagation speed of the front is by about 15 percent smaller compared to the wind speed shortly behind the front. The resulting velocity convergence near the front leads to an increasing vertical thickness of the frontal head. A part of the velocity convergence is compensated by a divergence of the wind direction,

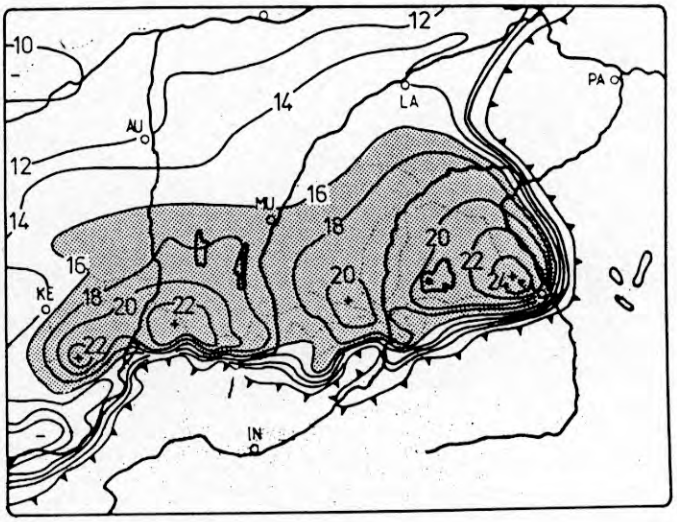

a)

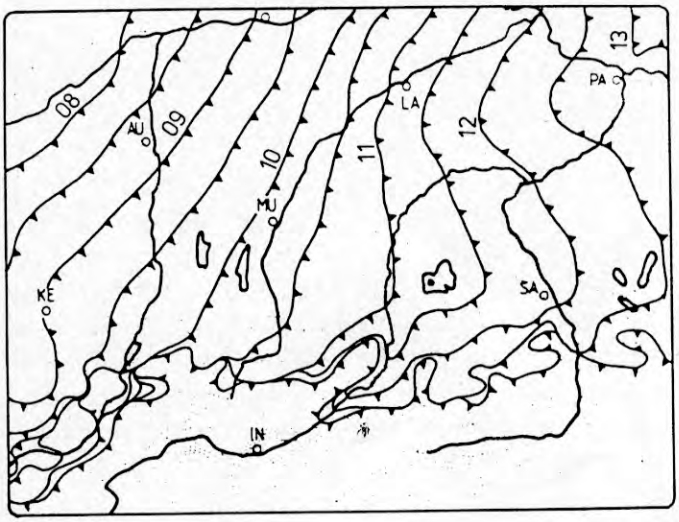

b)

Figure 9 Model domain C, 3 May 1987, 12 UTC, run I: (a) Top: Simulated velocity within model layer 1 ($|\vec{v}_{1,I}|$ in m/s). (b) Bottom: Half hourly isochrones of the simulated positions of Front 1 between 08 and 13 UTC.

which enlarges the frontal head towards the north after 11 UTC.

3.4 Theoretical Aspects

In order to classify the behaviour of a cold front near mountains Davies (1984) used dimensionless parameters. He found that small values of the rotational Froude number and of the height aspect ratio are favorable for the orographic retardation of a cold front. An extended set of dimensionless parameters was defined by Schumann (1987). Although not all of these numbers will be discussed below, the same set is evaluated for run I to enable a comparison with Schumann's classification of numerically simulated, idealized cold fronts:

Froude number	$Fr = U/c$
rotational Froude number	$\epsilon = L/R$
Rossby number	$Ro = Fr/\epsilon$
height aspect ratio	$N_0 = \Delta h_1/H$
ratio of inertia to Coriolis force	$N_1 = Fr^2/\epsilon$
ratio of kinetic to potential energy	$N_2 = 0.5\ Fr^2\ \Delta h_1/H$
ratio of mountain to frontal steepness	$N_3 = (HR)/(\Delta h_1 L)$

The numbers are calculated by the following physical parameters:

reduced acceleration of gravity	$g' = g\,(\Theta_2 - \Theta_1)/\Theta_2$
phase velocity of gravity waves	$c = \sqrt{g'\,\Delta h_1}$
Rossby radius	$R = c/f$
mountain height scale	H
mountain length scale	L
velocity scale	U

Since the scales depend on the spatial resolution they are determined separately for model domains A (synoptic scale) and B (mesoscale-α). They are listed in Table 2.

The resulting physical parameters and numbers are summarized in Table 3. The numbers predict a blocking of the cold air flow by the Alps: The mountains are steeper than the frontal face ($N_1 > 1$) and the kinetic energy of the cold air is insufficient to be converted

Table 2 Specification of characteristic measures of run I in the synoptic scale (taken from model domain A) and the mesoscale-α (taken from model domain B), respectively.

	synoptic scale	mesoscale-α
H	2 km	2 km
L	100 km	100 km
U	10 m/s	10 m/s
Δh_1	3000 m	500 m
$\Delta\Theta_1$	13 K	13 K

Table 3 Parameters and non-dimensional numbers for run I in the synoptic scale (taken from model domain A) and the mesoscale-α (taken from model domain B), respectively.

	synoptic scale	mesoscale-α
g'	0.4 m/s^2	0.4 m/s^2
c	35 m/s	15 m/s
R	350 km	150 km
Fr	0.3	0.7
ϵ	0.3	0.7
Ro	1	1
N_0	1.5	0.25
N_1	0.3	0.7
N_2	0.0675	0.05
N_3	2.3	6

to the amount of potential energy which is necessary to cross the Alps ($N_2 \ll 1$). The synoptic-scale Rossby radius R = 350 km suggests that the Alps influence the flow up to this distance. This is confirmed by the difference vectors which almost vanish 350 km away from the Alps (upper boundary of Figure 7a).

Looking at the mesoscale-α the mountains even act like a wall ($N_3 \gg 1$), and the cold air approaches the Alps in a very shallow layer. Thus, we have to expect a very dramatic modification of the front within a distance of R = 150 km off the mountain rim. This is in agreement with the observations (Figure 4b) as well as with the model results (Figure 9).

If stationarity is assumed the mountain-parallel propagation speed of the leading edge of a density current in a rotational system is given by Stern et al. (1982):

$$c_F = 0.5\, u_\infty + g' \frac{h_\infty}{u_\infty} \qquad (10)$$

u_∞ and h_∞ are the values 'far behind the front' of the crossfrontal wind component and the cold air thickness, respectively. For u_∞ = 16 m/s and h_∞ = 700 m (corresponding to u_1 and Δh_1 simulated for 12 UTC in a distance of 150 to 200 km behind the front) Equation 10 predicts $c_F \approx 25$ m/s. This value does not differ much from the simulated progression speed of the front (21 m/s), although the orographic jet is evidently instationary.

3.5 Importance of Diabatic Processes

The simple three-layer model, of course, only gives estimates about the consequences of the diabatic processes. The simulated amounts of precipitation merely reached ten percent of those observed. This is due to the coarse vertical resolution of the model and the rather simple treatment of humidity effects (see Section 2.3), which allows for neither convective precipitation nor diabatic effects of melting snow to be simulated. However, both processes seem to be important in the real case of the 'papal front'. Therefore, the present model is used to assess the qualitative rather than the quantitative effects of diabatic processes.

The model results confirm the assumption that a diabatic cooling due to partly evaporating rain might have caused the development of a second front line. Figure 10a shows the difference of potential temperatures in layer 1 between model run I with diabatic processes and run III without diabatic processes ($\Theta_{1,I} - \Theta_{1,III}$). Due to evaporating rain the air of layer 1 was cooled by up to 1.5 K within the precipitation area over southwestern Germany. However, a temperature drop of 6 K was observed in this region near the ground as depicted in Figure 4a. This discrepancy does not surprise. The

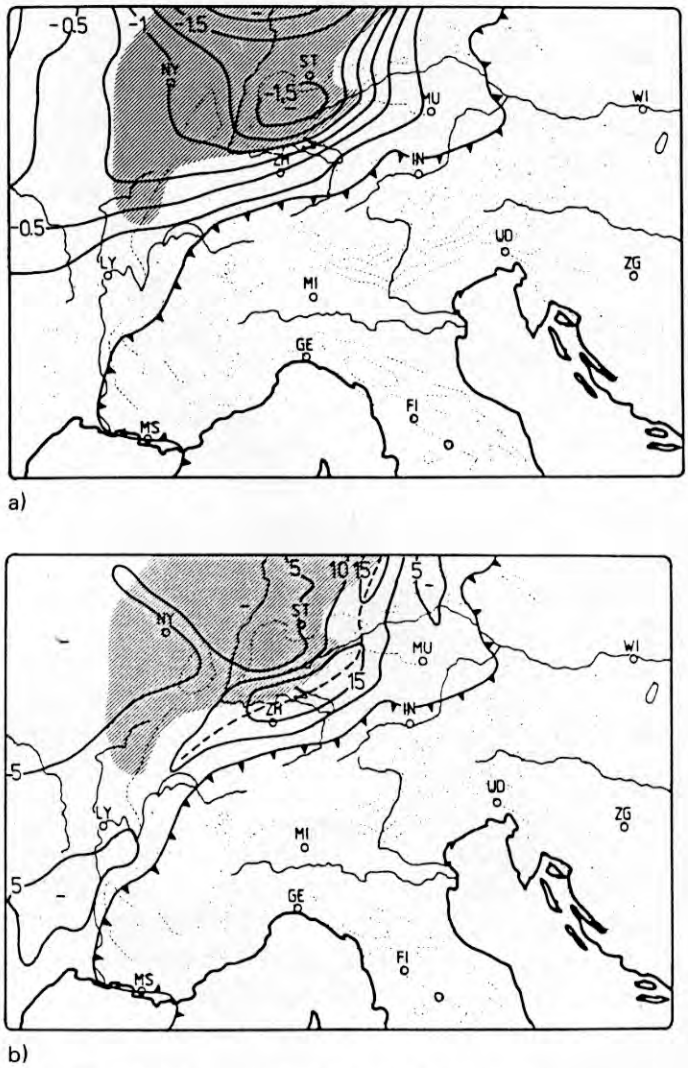

Figure 10 Model domain B, 3 May 1987, 12 UTC.
(a) Top: Difference of the potential temperatures within the lowest model layer between the runs I and III ($\Theta_{1,I} - \Theta_{1,III}$ in K).
Hatched area: region with an amount of simulated precipitation of 0.1 mm or more between 06 and 12 UTC.
(b) Bottom: Solid isolines: horizontal gradient of potential temperature within the lowest model layer ($|\nabla_h \Theta_{1,I}|$ in mK/km) as simulated in run I.
Broken line: maximum line of the horizontal gradient of potential temperature. Hatched area: region with an amount of simulated precipitation of 0.1 mm or more between 06 and 12 UTC.

postfrontal radiosounding of Nancy (12 UTC) suggests that the cooling increased towards the earth's surface. On the contrary, the model homogeneously distributes the cooling over the vertical extent of the lowest model layer. The underestimated precipitation rate in the model may also explain the only little cooling effect. Though, one has to keep in mind that the diabatic cooling is not strictly proportional to the precipitation rate. It ceases as soons as the model layer gets saturated by the evaporated rain. Nevertheless, the model generates a sharp horizontal gradient of potential temperature ($\nabla_h \Theta_1$) at the leading edge of the precipitation area

within layer 1 (Figure 10b). We relate the line of maximum temperature gradient with the observed Front 2. Note that model Front 2 does not correspond with an intersecting line of a model surface with the ground like Front 1. It is rather represented as an internal front within the lowest model layer. Run III did not produce a sharp horizontal gradient of the potential temperature within layer 1. In this run the values of $\nabla_h\Theta_1$ remain homogeneously distributed and lie at about 5 mK/km at 12 UTC as they were initialized at 00 UTC.

Diabatic effects cannot only generate a front, they can also intensify an existing frontal system. This was predicted by Hsie et al. (1984), for instance, who evaluated model simulations of frontogenesis in a moist atmosphere. The essential mechanism is the release of latent heat by condensation aloft and the consumption of sensible heat by evaporation near the ground. The corresponding heating and cooling increase the cross-frontal temperature gradient and result in a stronger static stability. This intensifies the ageostrophic circulations around the frontal zone and accelerates the surface cold front.

Accordingly, model runs I and III show that diabatic effects increase the difference of potential temperatures between layers 1 and 2 ($\Delta\Theta_1 = \Theta_2 - \Theta_1$) by about 30 percent. Relative to the dry case the Rossby radius R increases by 14 % while both, the Froude number Fr and the rotational Froude number ϵ, decrease by 12 %. The ratio of kinetic energy to potential energy (N_2) even deminuishes by 22 %. By and large, the diabatic processes favour the blocking of the cold air at the Alps. They intensify the mountain parallel wind component, i.e. the orographic jet.

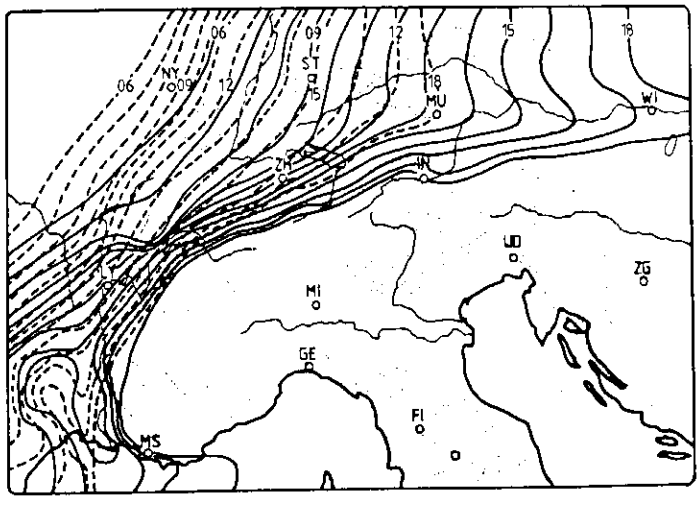

Figure 11 Model domain B, 3 May 1987: Hourly isochrones (06 – 18 UTC) of the 12 °C isoline of model run I with diabatic processes (dashed). The numbers indicate UTC hours.

The propagation of the cold air is depicted by hourly isochrones of the 12 °C potential temperature isolines for runs I and III in Figure 11. In run I the 12 °C line is situated very close to the line of maximum horizontal gradient of Θ_1, and can be related to the respective location of Front 2. Already at 06 UTC, when domain B was initialized, the 12 °C isoline of run I is situated 100 km farther east. During the following hours this line proceeds much faster in run I than it does in run III. Until 12 UTC this is mainly due to the continuing diabatic cooling which causes the isotherms to move faster than the advecting speed. Note that isentrops are not material lines if diabatic processes are turned on. After 12 UTC the 12 °C isoline strongly accelerates along the Alps in run I. Even without considering diabatic processes this isoline speeds up so that at 18 UTC the isoline of run III moves as fast as that of run I already at 12 UTC. The distance of the isochrones has increased to almost 450 km by 18 UTC.

4 Conclusions

The numerical imitations of the 'papal front' case reveal the influences on the frontal behaviour of both the Alpine orography and the diabatic heat exchange. The mountains block the southeastward penetration of the cold air and lead to the formation of an orographic jet, i.e. an along-barrier belt of high wind speeds with a nose-like deformation of the front. The diabatic cooling within the precipitation area ahead of the eastward moving trough acts frontogenetic, inducing a second front line. The model result suggest that an orographic jet has been formed behind the synoptic-scale Front 1 after 11 UTC independently on whether diabatic processes were invoked or not. At this stage we have to point to a discrepancy between the model results and the reality. After 10 UTC the preceding Front 1 was observed to be almost stationary while the orographic jet developed behind Front 2. Only when the faster Front 2 has merged into Front 1 at about 15 UTC near Salzburg the model conforms with the reality. However, the simulations give evidence that the synoptic weather situation of that day was predestinated for the generation of an orographic jet.

The 'papal front' simulations have shown that the simple conception of the three-layer shallow water model FRONTOM is altogether adequate to answer principle questions concerning the impact of orography on fronts. Especially, the employed nesting method ensures the consistancy of simulated mesoscale features with their synoptic-scale environment. However, the vertical resolution of the model is too coarse to describe mesoscale structures in detail. In particular,

diabatic processes can be imitated only with great caution. Hence, simulations on a fully three-dimensional grid are necessary if special effects are to be investigated. This includes convective precipitation at fronts and frontal rainbands, for instance. Especially the observation periods of 12 November, 13 November, and 19 December of the German Front Experiment 1987 (Hoinka et al., 1988) are very promising in respect to such tasks. It is hoped that numerical simulations of the experiment cases will lead to further knowledge of the combined influences of orography and diabatic processes on fronts and their scale interactions.

References

Baines, P.G., 1980: The Dynamics of the Southerly Buster. Austr. Meteor. Mag. **28**, 175–200

Ball, F.K., 1960: A Theory of Fronts in Relation to Surface Stress. Quart. J.R.Met. Soc. **96**, 51–66

Clark, L.T. and *R.D. Farley*, 1984: Severe Downslope Windstorm Calculations in Two and Three Spatial Dimensions Using Anelastic Interactive Grid Nesting: A Possible Mechanism for Gustiness, J. Atmos. Sc. **41**, 329–350

Colquhoun, J.R., D.J. Shepherd, C.E. Coulman, R.K. Smith, and *K. McInnes*, 1985: The Southerly Burster of South Eastern Australia: An Orographically Forced Cold Front. Mon. Wea. Rev. **113**, 2090–2107

Davies, H.C., 1984: On the Orographic Retardation of a Cold Front. Beitr. Phys. Atmosph. **57**, 409–418

Egger, J. and *K. Haderlein*, 1987: Fronts Near Orography in a One-Layer Model. J. Met. Soc. Japan, spec. Vol., Coll. pap. WMO/IUGG NWP Symp. Tokyo, 4–8 August 1986, p. 757–766

Egger, J., 1987: Distortion of Fronts Near Orography. Meteorol. Rdsch. **40**, 141–146

Egger, J., 1988: Frictionally Induced Circulation in Fronts. Beitr. Phys. Atmosph. **61**, 140–142

Garratt, J.R., 1986: Boundary-Layer Effects on Cold Fronts at a Coastline. Boundary-Layer Meteor. **36**, 101–105

Grammeltvedt, A., 1970: Numerical Simulation of the Motion of Atmospheric Fronts Using a Two Layer Model. Tellus **22**, 627–637

Haderlein, K., 1986: Numerische Modellrechnungen zum Verlagerungsverhalten orographisch modifizierter Kaltfronten Diplomarbeit, Meteorol. Inst. Univ. München

Heimann, D. and *H. Volkert*, 1988: The 'Papal Front' of 3 May 1987 – Mesoscale Analyses of Routine Data. Beitr. Phys. Atmosph. **61**, 62–68

Hoinka, K.P. and *D. Heimann*, 1988: Orographic Channelling of a Cold Front at the Pyrenees. Mon. Wea. Rev., **116**, 1817–1823

Hoinka, K.P., H. Volkert, and *D. Heimann*, 1988: The German Front Experiment 1987: Observations and Preliminary Results. DFVLR-Forschungsbericht, 88–21, obtainable from Wissenschaftliches Berichtswesen der DFVLR, P.O.B. 906058, D-5000 Köln 90, FRG

Hsie, E.-Y., R.A. Anthes and *D. Keyser*, 1984: Numerical Simulation of Frontogenesis in a Moist Atmosphere. J. Atmos. Sci. **41**, 2581–2594

Kasahara, A., E. Isaacson and *J.J. Stocker*, 1965: Numerical Studies of Frontal Motion in the Atmosphere I. Tellus **17**, 261–276

Kurz, M., 1982: Zum Einfluß diabatischer Prozesse auf die Frontogenese in Bodennähe. Meteorol. Rdsch. **35**, 21–30

Orlanski, I., 1975: A Rational Subdivision of Scales for Atmospheric Processes. Bull. Amer. Meteor. Soc. **56**, 527–534

Parish, T., 1982: Barrier Winds along the Sierra Nevada Mountains. J. Appl. Meteor. **21**, 925–930

Schumann, U., 1987: Influence of Mesoscale Orography on Idealized Cold Fronts. J. Atmos. Sci. **44**, 3423–3441

Steinacker, R., 1987: Orographie und Fronten. Wetter und Leben **39**, 65–70

Stern, M.E., Whitehead, J.A. and *B.-L., Hua*, 1982: The Intrusion of a Density Current Along the Coast of a Rotating Fluid. J. Fluid Mech. **123**, 237–265

Zhang, D.-L., H.-R. Chang, N.L. Seaman, T.T. Warner and *J.M. Fritsch*, 1986: A Two-Way Interactive Nesting Procedure with Variable Terrain Resolution. Mon. Wea. Rev. **114**, 1330–1339